



# Analytical Gaussian process cosmography: unveiling insights into matter-energy density parameter at present

Bikash R. Dinda<sup>1,2,a</sup>

<sup>1</sup> Department of Physical Sciences, Indian Institute of Science Education and Research Kolkata, Mohanpur, Nadia, West Bengal 741246, India

<sup>2</sup> Department of Physics and Astronomy, University of the Western Cape, Cape Town 7535, South Africa

Received: 13 February 2024 / Accepted: 7 April 2024 / Published online: 18 April 2024  
© The Author(s) 2024

**Abstract** In this study, we introduce a novel analytical Gaussian Process (GP) cosmography methodology, leveraging the differentiable properties of GPs to derive key cosmological quantities analytically. Our approach combines cosmic chronometer (CC) Hubble parameter data with growth rate ( $f$ ) observations to constrain the  $\Omega_{m0}$  parameter, offering insights into the underlying dynamics of the Universe. By formulating a consistency relation independent of specific cosmological models, we analyze under a flat FLRW metric and first-order Newtonian perturbation theory framework. Our analytical approach simplifies the process of Gaussian Process regression (GPR), providing a more efficient means of handling large datasets while offering deeper interpretability of results. We demonstrate the effectiveness of our methodology by deriving precise constraints on  $\Omega_{m0}h^2$ , revealing  $\Omega_{m0}h^2 = 0.139 \pm 0.017$ . Moreover, leveraging  $H_0$  observations, we further constrain  $\Omega_{m0}$ , uncovering an inverse correlation between mean  $H_0$  and  $\Omega_{m0}$ . Our investigation offers a proof of concept for analytical GP cosmography, highlighting the advantages of analytical methods in cosmological parameter estimation.

## 1 Introduction

In 1998, observations of type Ia supernovae provided compelling evidence for the current accelerated expansion of the Universe, marking the onset of late-time cosmic acceleration [1–8]. Subsequent observations, including those of the cosmic microwave background (CMB) [9–11], cosmic chronometers (CC) measuring the Hubble parameter [12–14], and baryon acoustic oscillations (BAO) [15–17], have independently confirmed this accelerated expansion. The prevailing explanation for this phenomenon revolves around

two main classes of models: one posits the existence of dark energy, a component with a large negative pressure driving the acceleration [18–23]; the other considers modifications to the general theory of relativity on cosmological scales [24–36]. Among these models, the  $\Lambda$ CDM model stands out as the most popular and successful [37]. In  $\Lambda$ CDM, the cosmological constant is identified as the leading candidate for dark energy, providing a robust framework for understanding the observed cosmic acceleration.

Despite the considerable success of the  $\Lambda$ CDM model, it grapples with both theoretical and observational challenges. Theoretical concerns include issues of fine-tuning and the cosmic coincidence problem [38–41]. On the observational front, the model exhibits discrepancies in derived quantities such as  $H_0$  (the present Hubble parameter) [42–45] and  $\sigma_8$  parameters, particularly between early-time observations like the CMB and late-time measurements such as local determinations of  $H_0$  and cosmic shear observations of  $\sigma_8$  [46–50]. These inconsistencies have spurred investigations beyond the  $\Lambda$ CDM paradigm.

Efforts to address these challenges have led to explorations of alternative models, including dynamical dark energy models [21] and early dark energy models [47]. While these models have shown success to a certain extent, concrete solutions to the identified problems remain elusive. Consequently, in recent times, there has been a shift towards model-independent and non-parametric approaches in the analysis [51–59]. These approaches aim to explore and study various cosmological observables, such as the Hubble parameter [52, 53] and the deceleration parameter [54–57], without being constrained by specific theoretical frameworks.

In the literature, certain parametric approaches are colloquially labeled as 'model-independent' because these parametrizations ostensibly avoid explicit dependence on specific cosmological models [45, 60]. An illustrative example is the cosmographic approach, which characterizes the

<sup>a</sup> e-mail: bikashd18@gmail.com (corresponding author)

expansion of the universe through distinct redshift or time derivatives of the scale factor or Hubble parameters [60]. However, it is essential to discern that these parametrizations, though not directly rooted in particular cosmological models, can themselves be considered models.

In this study, when we refer to model-independent analysis, we explicitly denote an approach that is truly free from reliance on any particular theoretical model or parametrization. While acknowledging the necessity of foundational concepts such as the existence of standard candles, our pursuit of model independence extends to a genuine absence of reliance on any cosmological model governing background expansion or the evolution of inhomogeneities, whether at the first order or even at higher-order perturbations [61–65].

To adapt the model-independent methodology, we use posterior Gaussian process regression (GPR) analysis [58, 59, 61, 66–81]. GPR is a powerful statistical technique used in various fields, including cosmology, to model complex data relationships. In the context of cosmography, GPR enables the reconstruction of cosmological observables, such as the Hubble parameter and the growth rate of cosmic structures, from observational data. Traditionally, GPR involves numerically sampling the Gaussian processes, which can be computationally intensive, especially with large datasets. However, with advancements in analytical methods, such as the analytical Gaussian process, we can now perform GPR more efficiently [70].

The analytical approach offers several advantages over numerical methods. Firstly, it simplifies the computational burden by avoiding the need for extensive numerical sampling. This makes it particularly advantageous for handling large cosmological datasets, where computational efficiency is crucial. Secondly, analytical GPR provides insights into the underlying data relationships in a more interpretable manner, facilitating a deeper understanding of cosmological phenomena [68–70].

Despite its benefits, analytical GPR also imposes constraints on the data that can be effectively fitted. These constraints arise from the assumptions inherent in the analytical framework and must be carefully considered to ensure the reliability of the results. Therefore, while analytical GPR offers a promising avenue for cosmography, it requires careful validation and verification to ensure its applicability to specific datasets [61, 80, 81].

Overall, the integration of analytical GPR into cosmological methodologies represents a significant advancement in our ability to extract meaningful insights from observational data. By leveraging the simplicity and efficiency of analytical techniques, we can enhance the accuracy and robustness of cosmological parameter estimation, ultimately advancing our understanding of the universe's fundamental properties and evolution [68–70].

Cosmological observations offer valuable insights, shedding light not just on the late-time cosmic acceleration but also on the current composition of the Universe. Currently, dark energy constitutes approximately 70% of the total energy budget, with total matter contributing around 30%. This distribution implies a present matter energy density parameter, denoted as  $\Omega_{m0}$ , of approximately 0.3 [9–11].

However, asserting  $\Omega_{m0} \approx 0.3$  lacks the straightforwardness of the evidence for late-time cosmic acceleration in terms of model-independent analysis. The dominance of dark energy in the late stages of the Universe's evolution sufficiently explains the observed acceleration. Determining cosmological quantities such as the deceleration parameter ( $q$ ) or the Hubble parameter ( $H$ ) in a model-independent manner can be achieved through a single type of cosmological observation or by cross-calibrating different datasets [61, 82].

For instance,  $H$  can be derived exclusively from cosmic chronometer observations, while  $q$  can be obtained from the derivative of the Hubble parameter data, provided the derivative is computed using model-independent techniques [58, 59]. However, many background cosmological observations predominantly involve the Hubble parameter or cosmological distances, like the luminosity distance. Relying solely on a single type of observation or calibration between them is insufficient to determine the precise value of  $\Omega_{m0}$ . This limitation arises because neither the Hubble parameter nor cosmological distances trace the individual energy budget of each constituent in the Universe.

Cosmological observations closely associated with the growth rate, denoted as  $f$ , of matter inhomogeneities, play a crucial role in determining the value of the  $\Omega_{m0}$  parameter [61–64]. This study aims to integrate these observations with background cosmological data, particularly insights from cosmic chronometers. The goal is to ascertain  $\Omega_{m0}$  in a manner independent of specific models. This approach becomes feasible as we will demonstrate that the equation governing the evolution of inhomogeneity growth explicitly features the  $\Omega_{m0}$  parameter.

The paper is structured as follows: Sect. 2 outlines the redshift evolution of the matter-energy density parameter. Section 3 derives the first-order perturbation theory equation for the matter growth rate. Section 4 details the expression for uncertainty propagation. Section 5 briefly discusses cosmic chronometers and growth rate data. Section 6 delves into the methodology of Gaussian process regression analysis. Section 7 presents the constraints on the present matter energy density parameter. Finally, Sect. 8 concludes the study.

## 2 Matter energy density parameter

We posit that at late times, the Universe is predominantly governed by matter and dark energy. In this context, 'mat-

ter’ encompasses both cold dark matter and baryons. Additionally, we assume that there is no interaction between dark energy and matter. With these considerations and under the assumption of a flat Friedmann–Lemaître–Robertson–Walker (FLRW) metric for the background expansion of the Universe, the evolution of the background matter energy density, denoted as  $\bar{\rho}_m$ , is derived as follows

$$\bar{\rho}_m = \bar{\rho}_{m0}(1+z)^3, \tag{1}$$

where  $\bar{\rho}_{m0}$  represents the current value of the matter-energy density, and  $z$  denotes the redshift. Using the above equation, the evolution of the matter-energy density parameter is expressed as [72]

$$\Omega_m = \frac{\bar{\rho}_m}{3M_{pl}^2 H^2} = \frac{\bar{\rho}_{m0} H_0^2 (1+z)^3}{3M_{pl}^2 H_0^2 H^2} = \frac{\Omega_{m0} H_0^2 (1+z)^3}{H^2}, \tag{2}$$

where  $H$  represents the Hubble parameter, and  $H_0$  is its current value. The reduced Planck mass is denoted as  $M_{pl}$ , while  $\Omega_{m0}$  signifies the present value of the matter-energy density parameter.

### 3 Growth of matter inhomogeneities

In the sub-Hubble limit and within the linear regime, employing first-order linear Newtonian perturbation theory allows us to investigate the evolution of perturbations in the Universe. In this context, the differential equation governing the growth of matter inhomogeneity, denoted as  $\delta_m$ , is presented as [22, 23, 72, 83, 84]:

$$\ddot{\delta}_m + 2H\dot{\delta}_m - 4\pi G\bar{\rho}_m\delta_m = 0, \tag{3}$$

where the overhead dot and double-dot signify first and second-order differentiations with respect to cosmic time  $t$ , and  $G$  represents the Newtonian gravitational constant. The differential equation above yields two solutions for  $\delta_m$ : one associated with the growing mode and the other with the decaying mode. Our focus is on the growing mode solution, denoted as  $D_+$ . This  $D_+$  follows the same differential equation as in Eq. (3).

We use the notation  $Q' = \frac{dQ}{dz}$  and  $Q'' = \frac{d^2Q}{dz^2}$ , where primes and double primes represent first and second-order differentiations with respect to redshift  $z$ . Utilizing the relations  $\dot{D}_+ = -(1+z)HD'_+$ ,  $\ddot{D}_+ = (1+z)^2 H^2 [D''_+ + (1 + \frac{1+z}{H} H')D'_+]$ , and  $8\pi G = M_{pl}^{-2}$ , we express the differential equation for  $D_+$  as

$$(1+z)^2 D''_+ + (1+z) \left( \frac{1+z}{H} H' - 1 \right) D'_+ - \frac{3}{2} \Omega_m D_+ = 0. \tag{4}$$

In the context of cosmic structure formation, a crucial quantity is the logarithmic growth rate  $f$ , defined as

$$f = \frac{d \ln D_+}{d \ln a} = -\frac{1+z}{D_+} D'_+, \tag{5}$$

where  $a$  represents the cosmic scale factor, and its relationship with redshift is given by  $1+z = a^{-1}$ . The equation above can be reformulated as  $D'_+ = -\frac{D_+}{1+z} f$ . Differentiating this equation yields  $D''_+ = -\frac{D_+}{(1+z)^2} [(1+z)f' - f^2 - f]$ . Substituting these relations into Eq. (4), we obtain a differential equation for  $f$  given as [61]

$$(1+z)f' - f^2 + \left( \frac{1+z}{H} H' - 2 \right) f + \frac{3}{2} \Omega_m = 0. \tag{6}$$

This equation can be rearranged to explicitly express  $\Omega_m$  in terms of  $f$ ,  $f'$ , and other relevant quantities, as given below

$$\Omega_m = \frac{2}{3H} \left[ (2H - (1+z)H') f + Hf^2 - (1+z)Hf' \right]. \tag{7}$$

By equating Eqs. (2) and (7), an expression for  $\Omega_{m0} H_0^2$  emerges as

$$\Omega_{m0} H_0^2 = \frac{2H \left[ (2+f)Hf - (1+z)(H'f + Hf') \right]}{3(1+z)^3}. \tag{8}$$

From this equation, one can estimate the value of  $\Omega_{m0} H_0^2$  by knowing the values of  $H$ ,  $H'$ ,  $f$ , and  $f'$  at a specific redshift  $z$ .

### 4 Propagation of errors

Let us define

$$W_{m0} = \Omega_{m0} H_0^2. \tag{9}$$

The accuracy of the estimated  $W_{m0}$  using Eq. (8) is contingent upon the uncertainties in  $H$ ,  $H'$ ,  $f$ , and  $f'$ . To quantify this uncertainty, we employ the propagation of errors, expressed as

$$\begin{aligned} \text{Var}[W_{m0}] &= \left( \frac{\partial W_{m0}}{\partial H} \right)^2 \text{Var}[H] + \left( \frac{\partial W_{m0}}{\partial H'} \right)^2 \text{Var}[H'] \\ &+ 2 \left( \frac{\partial W_{m0}}{\partial H} \right) \left( \frac{\partial W_{m0}}{\partial H'} \right) \text{Cov}[H, H'] \\ &+ \left( \frac{\partial W_{m0}}{\partial f} \right)^2 \text{Var}[f] + \left( \frac{\partial W_{m0}}{\partial f'} \right)^2 \text{Var}[f'] \\ &+ 2 \left( \frac{\partial W_{m0}}{\partial f} \right) \left( \frac{\partial W_{m0}}{\partial f'} \right) \text{Cov}[f, f'], \end{aligned} \tag{10}$$

where  $\text{Var}[Q]$  denotes the variance in the quantity  $Q$ , and  $\text{Cov}[P, Q]$  represents the covariance between two quantities,  $P$  and  $Q$ . And we have

$$\frac{\partial W_{m0}}{\partial H} = \frac{4f^2H - 4H(z+1)f' - 2f(z+1)H' + 8fH}{3(z+1)^3}, \tag{11}$$

$$\frac{\partial W_{m0}}{\partial H'} = -\frac{2fH}{3(z+1)^2}, \tag{12}$$

$$\frac{\partial W_{m0}}{\partial f} = \frac{2H(2(f+1)H - (z+1)H')}{3(z+1)^3}, \tag{13}$$

$$\frac{\partial W_{m0}}{\partial f'} = -\frac{2H^2}{3(z+1)^2}. \tag{14}$$

It's important to note that in Eq. (10), we specifically account for the covariance between  $H$  and  $H'$ , as well as the covariance between  $f$  and  $f'$ , excluding other pairs. The rationale behind this selective consideration will be discussed in subsequent sections.

### 5 Observational data

In our investigation, we incorporate data from cosmic chronometer (CC) observations, comprising a comprehensive set of 32 Hubble parameter measurements distributed across a range of redshift values ( $0.07 \leq z \leq 1.965$ ). This dataset, as meticulously detailed in [14], plays a pivotal role in unraveling the intricacies of cosmic evolution. It's noteworthy that among these 32 Hubble parameter measurements, 15 exhibit correlations, and we judiciously integrate these covariances into our analytical framework,<sup>1</sup> enhancing the precision of our analysis. The mean values and standard deviations of the observed Hubble parameter can be found in Table 1. It's noteworthy that for the last 15 redshift points marked with asterisks, non-zero covariances are present.

We have plotted the observed Hubble parameter data, along with their associated errors represented by error bars, in Fig. 1.

Additionally, our study encompasses growth rate observations, as elucidated by [62]. These observations encapsulate a collection of 11 uncorrelated data points about the growth rate parameter  $f$  within the redshift range  $0.013 \leq z \leq 1.4$ . The table provided in Table 2 presents the mean values and standard deviations of the logarithmic growth rate  $f$ . In the corresponding table, the survey names and cosmological tracer labels are provided alongside the observed  $f$  values at various redshifts. It is assumed that within these data, there exists no correlation between different redshift points, or any existing correlations are deemed negligible.

We have plotted the logarithmic growth rate data, along with their associated errors represented by error bars, in Fig. 2.

<sup>1</sup> The covariances can be accessed at the following link: <https://gitlab.com/mmoresco/CCcovariance/> [85–88].

**Table 1** The Hubble parameter's observed values, along with their  $1\sigma$  uncertainties, are documented at 32 redshift points, specifically from cosmic chronometers (CC) observations. Notably, at 15 of these redshift points marked with asterisks, correlations exist among each pair of observations, indicating the presence of covariances

Sr. No	$z$	$H \pm \Delta H$ [km s <sup>-1</sup> Mpc <sup>-1</sup> ]	References
1	0.07	69.0 ± 19.6	[89]
2	0.09	69.0 ± 12.0	[90]
3	0.12	68.6 ± 26.2	[89]
4	0.17	83.0 ± 8.0	[90]
5	0.2	72.9 ± 29.6	[89]
6	0.27	77.0 ± 14.0	[90]
7	0.28	88.8 ± 36.6	[89]
8	0.4	95.0 ± 17.0	[90]
9	0.47	89.0 ± 50.0	[91]
10	0.48	97.0 ± 62.0	[92]
11	0.75	98.8 ± 33.6	[93]
12	0.88	90.0 ± 40.0	[92]
13	0.9	117.0 ± 23.0	[90]
14	1.3	168.0 ± 17.0	[90]
15	1.43	177.0 ± 18.0	[90]
16	1.53	140.0 ± 14.0	[90]
17	1.75	202.0 ± 40.0	[90]
18	0.1791*	74.91 ± 5.57	[85]
19	0.1993*	74.96 ± 6.37	[85]
20	0.3519*	82.78 ± 14.65	[85]
21	0.3802*	83.0 ± 14.3	[85]
22	0.4004*	76.97 ± 11.12	[85]
23	0.4247*	87.08 ± 12.47	[85]
24	0.4497*	92.78 ± 14.07	[85]
25	0.4783*	80.91 ± 10.23	[85]
26	0.5929*	103.8 ± 14.0	[85]
27	0.6797*	91.6 ± 9.5	[85]
28	0.7812*	104.5 ± 13.3	[85]
29	0.8754*	125.1 ± 17.1	[85]
30	1.037*	153.7 ± 20.4	[85]
31	1.363*	160.0 ± 32.9	[85]
32	1.965*	186.5 ± 49.8	[85]

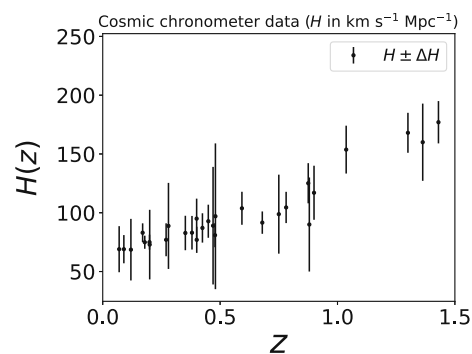


**Fig. 1** Observed Hubble parameter data from cosmic chronometer observations with associated error bars representing  $1\sigma$  uncertainties

**Table 2** The observed values of  $f$  along with their  $1\sigma$  uncertainties are documented at 11 redshift points, aligning with various survey data

Sr. No.	Survey Name	$z$	$f \pm \Delta f$	References	Cosmological tracers
1	ALFALFA	0.013	$0.56 \pm 0.07$	[94]	HI extragalactic sources
2	2dFGRS	0.15	$0.49 \pm 0.14$	[95,96]	galaxies
3	GAMA	0.18	$0.49 \pm 0.12$	[97]	multi-tracer: blue & red galaxies
4	WiggleZ	0.22	$0.60 \pm 0.10$	[98]	galaxies
5	SDSS	0.35	$0.70 \pm 0.18$	[99]	luminous red galaxies (LRG)
6	GAMA	0.38	$0.66 \pm 0.09$	[97]	multi-tracer: blue & red galaxies
7	WiggleZ	0.41	$0.70 \pm 0.07$	[98]	galaxies
8	2SLAQ	0.55	$0.75 \pm 0.18$	[100]	LRG & quasars
9	WiggleZ	0.60	$0.73 \pm 0.07$	[98]	galaxies
10	VIMOS-VLT Deep Survey	0.77	$0.91 \pm 0.36$	[96]	faint galaxies
11	2QZ & 2SLAQ	1.40	$0.90 \pm 0.24$	[101]	quasars

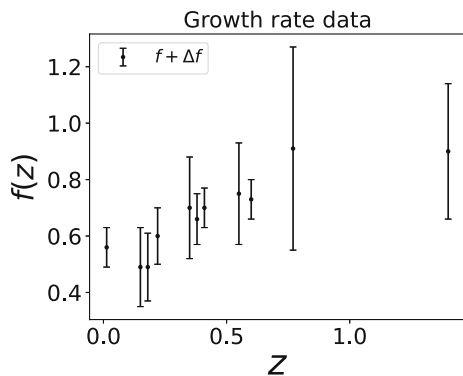


**Fig. 2** Logarithmic growth rate data with associated error bars representing  $1\sigma$  uncertainties

### 6 Methodology

We employ analytical (posterior approach) Gaussian process regression (GPR) analysis [58,59,61,66–81] to reconstruct  $H$  and  $H'$  at specific redshift points from the observed Hubble parameter data. Similarly, utilizing analytical GPR, we reconstruct  $f'$  at the same redshift points from the observed growth rate ( $f$ ) data. We utilize analytical GPR for its convenience in handling observational data linearly related to GPR. Initially, we determine the posterior distributions of  $H$ ,  $f$ , and their derivatives. Subsequently, we compute the mean and standard deviations at specific target redshift points, along with the covariances between each pair of these points. These computations are vital for determining  $W_{m0}$  i.e.  $\Omega_{m0}H_0^2$  through Eq. (8), where we require  $H$ ,  $f$ , and their derivatives at the same redshift points. We align the observed redshift points of the  $f$  data with our target redshift points of interest, except for the lowest redshift point ( $z = 0.013$ ). Particularly, we select 10 redshift points within the range  $0.15 \leq z \leq 1.4$  based on the  $f$  data, excluding the lowest one. These target redshift points are detailed in Table 3.

This selection is motivated by several considerations. Firstly, to calculate  $W_{m0}$  using Eq. (8), we require all four

**Table 3** Target redshift points

Sr. no.	Redshift point
1	0.15
2	0.18
3	0.22
4	0.35
5	0.38
6	0.41
7	0.55
8	0.60
9	0.77
10	1.40

quantities- $H$ ,  $H'$ ,  $f$ , and  $f'$ -to be available at the same redshift points. Secondly, the chosen redshift range is situated within both the redshift ranges of the  $H$  and  $f$  data and employing interpolation techniques such as GPR can yield reliable results when interpolating from a specified range of redshifts to a subset range of redshifts. Thirdly, we have the flexibility to select either the observed  $H$  data or the observed  $f$  data to directly substitute into Eq. (8) for computing  $\Omega_{m0}H_0^2$ . This approach allows us to incorporate at least one quantity directly obtained from observational data instead of relying solely on reconstructed values. For this purpose, we opt to use the observed  $f$  data in Eq. (8).

As mentioned earlier, in our investigation, we opt for the posterior approach of Gaussian process regression (GPR) analysis for its efficiency in computational time and straightforward applicability. Let's delve briefly into the workings of GPR analysis and its application in reconstructing a function and its derivatives, specifically the first order, at target points along with associated errors from a given dataset.

Consider a dataset featuring  $n$  observational data points denoted by vectors  $X$  and  $Y$ , representing observation coordinates and mean values of a quantity, respectively. The dataset also incorporates observational errors through the covariance

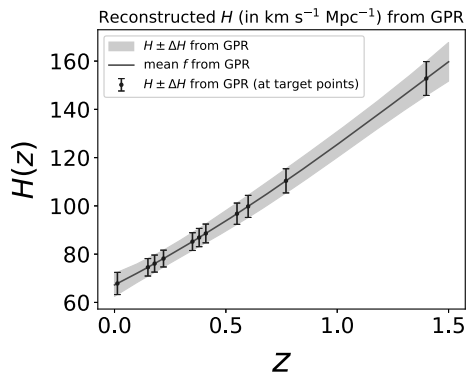


**Fig. 3** Reconstructed values of the Hubble parameter along with associated errors obtained from analytical Gaussian Process Regression (GPR). The green line and light-blue regions denote the mean function and  $1\sigma$  uncertainty region, respectively. Blue error bars represent the mean and standard deviation values of the reconstructed Hubble parameter at target redshift points mentioned in Table 3

matrix  $C$ , denoted as  $C = \text{Cov}[Y, Y]$ . GPR analysis facilitates the prediction of mean values and covariances for the same quantity at different target points  $X_*$ , represented by vectors  $Y_*$  and  $\text{Cov}[Y_*, Y_*]$ , leveraging a kernel covariance function and a mean function. In this context, we assume a zero mean function to eliminate model dependence, enhancing the versatility of our approach. The predicted values are computed through the expressions given by [66–69]:

$$Y_* = K(X_*, X) [K(X, X) + C]^{-1} Y, \quad (15)$$

$$\begin{aligned} \text{Cov}[Y_*, Y_*] &= K(X_*, X_*) \\ &- K(X_*, X) [K(X, X) + C]^{-1} K(X, X_*), \end{aligned} \quad (16)$$

where  $K$  is the kernel matrix based on a specific kernel covariance function. We adopt the squared-exponential kernel, where the covariance between two arbitrary points  $x_i$  and  $x_j$  is expressed as:

$$k(x_i, x_j) = \sigma_f^2 e^{-\frac{(x_i - x_j)^2}{2l^2}}, \quad (17)$$

where  $\sigma_f$  and  $l$  are the corresponding kernel hyperparameters, and we incorporate optimal values for these hyperparameters in predictions for Eqs. (15) and (16). Determining these optimal values involves minimizing the negative log marginal likelihood ( $\log P(Y|X)$ ), as presented in [68]:

$$\begin{aligned} \log P(Y|X) &= -\frac{1}{2} Y^T [K(X, X) + C]^{-1} Y \\ &- \frac{1}{2} \log |K(X, X) + C| - \frac{n}{2} \log (2\pi), \end{aligned} \quad (18)$$

where  $|K(X, X) + C|$  represents the determinant of the  $K(X, X) + C$  matrix.

In Fig. 3, we have plotted the reconstructed values of the Hubble parameter and the associated errors obtained from analytical GPR. The green line and the light-blue regions

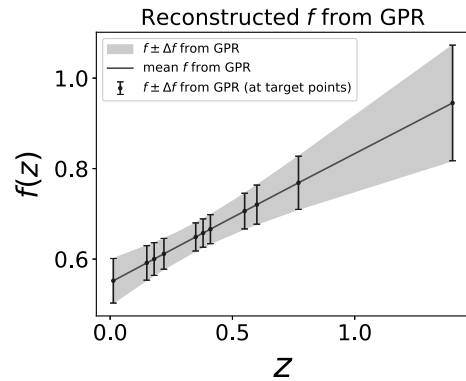


**Fig. 4** The reconstructed values of the logarithmic growth rate ( $f$ ) obtained from analytical Gaussian Process Regression (GPR) analysis. The green line represents the mean function, while the light-blue regions indicate the  $1\sigma$  uncertainty region. Blue error bars depict the mean and standard deviation values of the reconstructed  $f$  at the specified target redshift points mentioned in Table 3

represent the corresponding mean function and the  $1\sigma$  uncertainty region, respectively. The blue error bars represent the mean and standard deviation values of the reconstructed Hubble parameter at the target redshift points mentioned in Table 3.

In Fig. 4, we have plotted the reconstructed values of  $f$  and the associated errors obtained from the analytical GPR analysis. The green line and the light-blue regions represent the corresponding mean function and the  $1\sigma$  uncertainty region, respectively. The blue error bars represent the mean and standard deviation values of the reconstructed  $f$  at the target redshift points mentioned in Table 3.

Furthermore, GPR extends its predictive capabilities to the gradient of a quantity. The mean vector and covariance matrix corresponding to the first derivative are articulated by [68]:

$$Y'_* = [K'(X, X_*)]^T [K(X, X) + C]^{-1} Y, \quad (19)$$

$$\begin{aligned} \text{Cov}[Y'_*, Y'_*] &= K''(X_*, X_*) \\ &- [K'(X, X_*)]^T [K(X, X) + C]^{-1} K'(X, X_*), \end{aligned} \quad (20)$$

where prime and double prime denote the first and second derivatives, respectively.  $k'(x, x_*)$  and  $k''(x_*, x_*)$  represent the partial derivatives of the kernel function:

$$\begin{aligned} k'(x, x_*) &= \frac{\partial k(x, x_*)}{\partial x_*}, \\ k''(x_*, x_*) &= \frac{\partial^2 k(x_*, x_*)}{\partial x_* \partial x_*}, \end{aligned} \quad (21)$$

where the notation  $k$  denotes the matrix element of the main matrix  $K$ . Additionally, the covariance matrix between the quantity and its first derivative is given by [68]:

$$\begin{aligned} \text{Cov}[Y_*, Y'_*] &= K'(X_*, X_*) \\ &- [K(X, X_*)]^T [K(X, X) + C]^{-1} K'(X, X_*). \end{aligned} \quad (22)$$

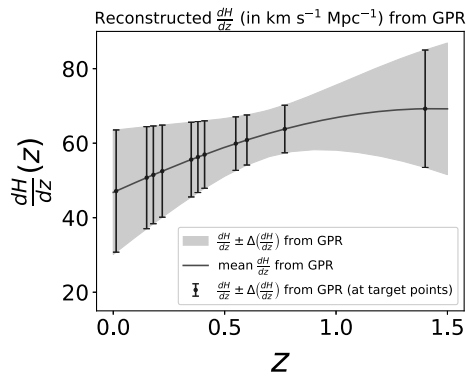


**Fig. 5** Reconstructed values of  $H'$  i.e.  $\frac{dH}{dz}$  obtained from analytical Gaussian Process Regression (GPR) analysis. The green line denotes the mean function, while the light-blue regions represent the  $1\sigma$  uncertainty region. Blue error bars indicate the mean and standard deviation values of the reconstructed  $H'$  at the specified redshift points mentioned in Table 3

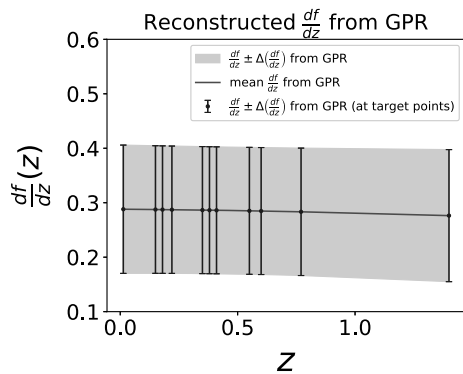


**Fig. 6** Reconstructed values of  $f'$ , denoted as  $\frac{df}{dz}$ , with associated errors. The green line represents the mean function, while the light-blue regions indicate the  $1\sigma$  uncertainty region obtained through analytical Gaussian Process Regression (GPR). Blue error bars denote the mean and standard deviation values of  $f'$  at specified redshift points mentioned in Table 3

In Fig. 5, we have plotted the reconstructed values of  $H'$  i.e.  $\frac{dH}{dz}$  and the associated errors obtained from analytical GPR. The green line and the light-blue regions represent the corresponding mean function and the  $1\sigma$  uncertainty region, respectively. The blue error bars represent the mean and standard deviation values of the reconstructed  $H'$  at the target redshift points mentioned in Table 3.

In Fig. 6, we present the reconstructed values of  $f'$  i.e.  $\frac{df}{dz}$  along with their associated errors obtained through analytical Gaussian Process Regression (GPR). The green line depicts the mean function, while the light-blue regions indicate the  $1\sigma$  uncertainty region. Blue error bars denote the mean and standard deviation values of the reconstructed  $f'$  at the specified redshift points mentioned in Table 3.

In summary, GPR proves to be a versatile tool, not only predicting the function and its derivatives but also providing insights into their covariations. This comprehensive predictive capability enhances the utility of GPR in our study, allowing for robust analyses and accurate reconstructions.

## 7 Results

After conducting GPR analysis, we now possess the reconstructed values of  $H, H', \text{Var}[H], \text{Var}[H'],$  and  $\text{Cov}[H, H']$  at each redshift point of interest, as mentioned earlier. Simultaneously, we have the reconstructed values of  $f, f', \text{Var}[f], \text{Var}[f'],$  and  $\text{Cov}[f, f']$ . Note that, we utilize the observed values of  $f$  and  $\text{Var}[f]$  in Eqs. (8) and (10) instead of their reconstructed counterparts from GPR. Although this step is not strictly necessary, it offers the advantage of incorporating true observational data directly, thereby mitigating potential errors that may arise during the reconstruction process, as mentioned earlier. However, a complication arises as follows: we need  $\text{Cov}[f, f']$  in Eq. (10) and we know these values between the reconstructed  $f$  and  $f'$  from GPR using Eq. (22), but we do not know the values if we use observed  $f$  instead of the reconstructed  $f$ . That means we do not know the covariances between the observed  $f$  and the reconstructed  $f'$ .

To address this issue, we assume that the normalized covariance between the observed  $f$  and the reconstructed  $f'$  is equivalent to that between the reconstructed  $f$  and the reconstructed  $f'$ . Here, the normalized covariance, denoted by  $\rho[f, f']$ , is defined as  $\text{Cov}[f, f'] = \rho[f, f'] \cdot \Delta f \cdot \Delta f'$ , where  $\Delta A$  represents the standard deviation of a quantity  $A$ , given by  $\Delta A = \sqrt{\text{Var}[A]}$ . We use the errors from the observed  $f$  data for  $\Delta f$  and the reconstructed values from GPR for  $\Delta f'$ . This approach enables us to obtain covariances between the observed  $f$  and the reconstructed  $f'$ .

The reconstruction of  $H$  and  $H'$ , as well as the reconstruction of  $f$  and  $f'$ , involves distinct datasets, leading to the absence of covariances between these two groups. Therefore, the only non-zero covariances are  $\text{Cov}[H, H']$  and  $\text{Cov}[f, f']$ . This explains why we have exclusively taken these two covariances into account in Eq. (10). However, it is important to note that this assumption may not hold strictly true because theoretically,  $H$  and  $f$  are related through Eq. (6), implying correlations between  $H, f,$  and their derivatives. However, in our simplified methodology utilizing posterior GPR analysis, where the observed data is linearly related to GPR, imposing such correlations would require multi-tasking of GPR, which is challenging. Therefore, for the sake of simplicity, we assume either no correlation or negligible correlation [81].

Finally, utilizing these computed values, we derive  $W_{m0}(z_i)$  and  $\Delta W_{m0}(z_i)$  at each redshift point  $z_i$  through Eqs. (8) and (10) respectively. From these results, we further obtain  $\Omega_{m0}h^2(z_i)$  and  $\Delta(\Omega_{m0}h^2)(z_i)$  at each redshift by applying the relations:

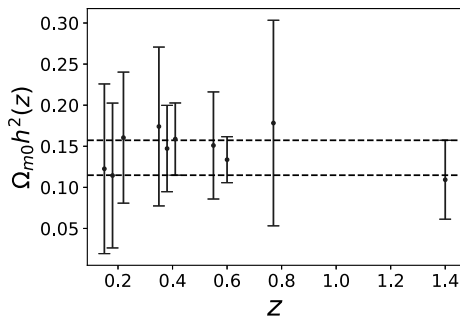


**Fig. 7** The reconstruction process yields values for  $\Omega_{m0}h^2(z_i)$  and  $\Delta(\Omega_{m0}h^2)(z_i)$  at 10 distinct redshift points denoted by  $z_i$ , depicted as blue error bars. The two horizontal dashed-black lines delineate the maximum allowable region for  $\Omega_{m0}h^2$  where all  $1\sigma$  error bars converge. The lower and upper horizontal black lines correspond to  $\Omega_{m0}h^2 \approx 0.115$  and  $\Omega_{m0}h^2 \approx 0.157$ , respectively

$$\Omega_{m0}h^2(z_i) = \frac{W_{m0}(z_i)}{10^4 (\text{km s}^{-1} \text{Mpc}^{-1})^2}, \tag{23}$$

$$\Delta(\Omega_{m0}h^2)(z_i) = \frac{\Delta W_{m0}(z_i)}{10^4 (\text{km s}^{-1} \text{Mpc}^{-1})^2}, \tag{24}$$

where we express the present value of the Hubble parameter as  $H_0 = 100 h \text{ km s}^{-1} \text{ Mpc}^{-1}$ .

In Fig. 7, the reconstructed values of  $\Omega_{m0}h^2(z_i)$  and  $\Delta(\Omega_{m0}h^2)(z_i)$  are depicted with blue error bars. The two horizontal dashed-black lines define the maximum region that all error bars commonly share. This region is crucial, as any single value of  $\Omega_{m0}h^2$  falling within it is supported by all 10 reconstructed values of  $\Omega_{m0}h^2(z_i)$  at a  $1\sigma$  confidence level. It's worth noting that the lower and upper horizontal black lines correspond to  $\Omega_{m0}h^2 \approx 0.115$  and  $\Omega_{m0}h^2 \approx 0.157$  respectively. At a  $2\sigma$  confidence level, this region would expand, and so forth.

According to the first-order Newtonian perturbations within the background FLRW metric,  $\Omega_{m0}h^2$  should be a constant. Therefore, if observations align completely with this underlying theory and the first-order Newtonian perturbation theory, the derived values of  $\Omega_{m0}h^2$  should be a constant regardless of the redshift point of the observed data. However, considering the presence of error bars, the data provides a region of possible values for  $\Omega_{m0}h^2$  at each observed redshift, depending on the confidence interval. At a specific confidence level, all observed regions of  $\Omega_{m0}h^2$  at different redshift points should intersect. The presence of an overlap region between the horizontal dashed-black lines in Fig. 7 confirms the consistency between the first-order Newtonian perturbations, the background FLRW metric, and the cosmic chronometers and growth rate data. This also underscores the utility of Eq. (8) for a simultaneous consistency test of the FLRW background metric and first-order Newtonian perturbations.

Given that the reconstructed values of  $\Omega_{m0}h^2(z_i)$  at each redshift  $z_i$  align with the notion that  $\Omega_{m0}h^2$  remains constant

**Table 4** The estimated value of the  $\Omega_{m0}h^2$  parameter and the associated  $1\sigma$  error

---


$$\Omega_{m0}h^2 = 0.139 \pm 0.017$$


---

across these points, we can view these reconstructions as 10 distinct measurements of the same quantity,  $\Omega_{m0}h^2$ , each with associated errors. With this interpretation, we employ standard parameter estimation techniques to calculate the  $\Omega_{m0}h^2$  parameter and its associated error. The mean value and variance of the  $\Omega_{m0}h^2$  parameter are computed using the following relations [102, 103]

$$\Omega_{m0}h^2 = \frac{\sum_i \frac{\Omega_{m0}h^2(z_i)}{\text{Var}[\Omega_{m0}h^2](z_i)}}{\sum_j \frac{1}{\text{Var}[\Omega_{m0}h^2](z_j)}}, \tag{25}$$

$$\text{Var}[\Omega_{m0}h^2] = \frac{1}{\sum_i \frac{1}{\text{Var}[\Omega_{m0}h^2](z_i)}}, \tag{26}$$

respectively and the standard deviation is determined as  $\Delta(\Omega_{m0}h^2) = \sqrt{\text{Var}[\Omega_{m0}h^2]}$ . These equations emphasize assigning higher weight to  $\Omega_{m0}h^2(z_i)$  with lower variance. The estimated value of  $\Omega_{m0}h^2$  and its associated  $1\sigma$  error are presented in Table 4.

Now to estimate the value of  $\Omega_{m0}$ , we have to break the degeneracy in  $\Omega_{m0}h^2$  by using the measured value of  $H_0$ . For the  $H_0$  value, we first compute it from the cosmic chronometer data itself. What we do we use the same procedure GPR analysis to compute  $H$  at  $z = 0$ . We find the value as  $H_0 = 67.2 \pm 4.7$ . We also consider two other values of  $H_0$  from two different observations. One is from the tip of the Red Giant Branch (tRGB) measurements which correspond to  $H_0 \approx 69.8 \pm 1.9$  [104]. The other one is from the SHOES measurement which corresponds to  $H_0 = 73.2 \pm 1.3$  [105]. From these  $H_0$  values, we compute  $h$  and  $\Delta h$  using the relations given as

$$h = \frac{H_0}{100 \text{ km s}^{-1} \text{ Mpc}^{-1}}, \tag{27}$$

$$\Delta h = \frac{\Delta H_0}{100 \text{ km s}^{-1} \text{ Mpc}^{-1}}, \tag{28}$$

respectively. Now, from the values of  $\Omega_{m0}h^2$ ,  $\Delta(\Omega_{m0}h^2)$ ,  $h$ , and  $\Delta h$ , we compute  $\Omega_{m0}$ ,  $\text{Var}[\Omega_{m0}]$  using the relations

$$\Omega_{m0} = \frac{(\Omega_{m0}h^2)}{h^2}, \tag{29}$$

$$\begin{aligned} \text{Var}[\Omega_{m0}] &= \left[ \frac{\partial \Omega_{m0}}{\partial (\Omega_{m0}h^2)} \right]^2 \text{Var}[\Omega_{m0}h^2] + \left[ \frac{\partial \Omega_{m0}}{\partial h} \right]^2 \text{Var}[h] \\ &= \frac{1}{h^4} \text{Var}[\Omega_{m0}h^2] + \frac{4(\Omega_{m0}h^2)^2}{h^6} \text{Var}[h], \end{aligned} \tag{30}$$

respectively and we find  $\Delta \Omega_{m0}$  as  $\Delta \Omega_{m0} = \sqrt{\text{Var}[\Omega_{m0}]}$ . We list all these estimated values in Table 5.

**Table 5** The estimated values of the  $\Omega_{m0}$  parameter and the associated  $1\sigma$  error correspond to three different sets of  $h$  and  $\Delta h$

Observation	$h \pm \Delta h$	$\Omega_{m0} \pm \Delta\Omega_{m0}$
CC (using GPR)	$0.672 \pm 0.047$	$0.308 \pm 0.057$
tRGB	$0.698 \pm 0.019$	$0.285 \pm 0.038$
SHOES	$0.732 \pm 0.013$	$0.259 \pm 0.033$

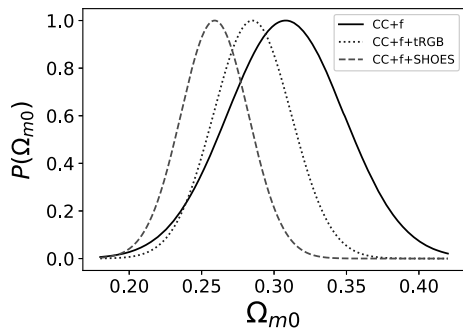


**Fig. 8** Probability distribution for  $\Omega_{m0}$ . The continuous black, dotted blue, and dashed red lines represent the constraints on  $\Omega_{m0}$  for the combinations of 'CC+f', 'CC+f+tRGB', and 'CC+f+SHOES' data sets, respectively

From the estimated values of the  $\Omega_{m0}$  and  $\Delta\Omega_{m0}$ , we plot the Gaussian probability distribution for  $\Omega_{m0}$  (denoted as  $P(\Omega_{m0})$ ) in Fig. 8. The solid-black, dotted-blue, and dashed-red lines correspond to the constraints on  $\Omega_{m0}$  for the combinations of 'CC+f', 'CC+f+tRGB', 'CC+f+SHOES' data sets respectively. We see that the higher the values of  $H_0$ , the lower the values of  $\Omega_{m0}$ .

### 8 Conclusion

In this investigation, we amalgamate Hubble parameter data from cosmic chronometers (CC) observations with growth rate data obtained from growth rate ( $f$ ) observations to derive constraints on the  $\Omega_{m0}$  parameter. Formulating a consistency relation for the combined parameter  $\Omega_{m0}h^2$  in terms of the Hubble parameter, its derivative, the growth rate ( $f$ ), and the derivative of  $f$  at a specific redshift  $z$ , we base our analysis on the assumption of a flat FLRW metric governing the background expansion of the Universe and the first-order Newtonian perturbation theory for the evolution of matter inhomogeneity. This relation serves as a valuable tool to scrutinize the consistency of the FLRW metric and first-order perturbations within the Newtonian perturbation theory, remaining independent of any particular cosmological model or parametrization.

Moreover, our investigation showcases the potential of analytical Gaussian Process (GP) cosmography as a valuable methodological advancement. By utilizing the differentiable

properties of GPs, we derive the necessary quantities analytically, offering significant computational advantages over traditional numerical methods. The analytical approach not only simplifies the computational burden but also provides deeper interpretability of results, facilitating a more comprehensive understanding of cosmological phenomena.

Employing Gaussian process regression (GPR) analysis, we compute the Hubble parameter, its derivative, and associated errors from cosmic chronometer observations. Similarly, we employ GPR to determine  $f$ ,  $f'$ , and their associated errors from growth rate measurements. Utilizing these reconstructed values in conjunction with the consistency relation, we constrain the  $\Omega_{m0}h^2$  parameter, resulting in  $\Omega_{m0}h^2 = 0.139 \pm 0.017$ .

Subsequently, leveraging  $H_0$  observations, we further constrain the  $\Omega_{m0}$  parameter. Initially, we use GPR to compute  $H_0$  directly from cosmic chronometer observations, yielding  $\Omega_{m0} = 0.308 \pm 0.057$  for  $H_0 = 67.2 \pm 4.7$ . We then consider the tip of the Red Giant Branch (tRGB) observation, corresponding to  $H_0 \approx 69.8 \pm 1.9$ , resulting in  $\Omega_{m0} = 0.285 \pm 0.038$ . Finally, utilizing the SHOES measurement of  $H_0$  ( $H_0 = 73.2 \pm 1.3$ ), we find  $\Omega_{m0} = 0.259 \pm 0.033$ . Notably, the study reveals an inverse correlation between the mean values of  $H_0$  and  $\Omega_{m0}$ .

In summary, this investigation confines the  $\Omega_{m0}$  parameter by integrating cosmic chronometers and growth rate observations, with or without additional Hubble constant measurements. Importantly, this is achieved in a completely cosmological model-independent manner, facilitated by the consistency relation governing the  $\Omega_{m0}h^2$  parameter. The model-independent methodology applied here, namely analytical Gaussian process cosmography, plays a crucial role in deriving constraints on  $\Omega_{m0}$  without reliance on specific cosmological models or parametrizations. By utilizing analytical Gaussian process regression to reconstruct cosmological observables, such as the Hubble parameter and growth rate, this approach ensures robust and interpretable results that align with the background FLRW metric and the first-order evolution of matter inhomogeneity in the Newtonian cosmological perturbation theory.

**Acknowledgements** The author would like to acknowledge IISER Kolkata for its financial support through the postdoctoral fellowship. The revision for this work was carried out during the author's tenure at UWC, partially supported by the South African Radio Astronomy Observatory and National Research Foundation (Grant no. 75415).

**Data availability statement** This manuscript has no associated data or the data will not be deposited. [Author's comment: This research uses publicly available cosmological data and wherever used cited properly.]

**Code availability statement** The manuscript has no associated code/software. [Authors comment: Code/Software sharing not applicable to this article as no code/software was generated or analysed during the current study.]

**Open Access** This article is licensed under a Creative Commons Attribution 4.0 International License, which permits use, sharing, adaptation, distribution and reproduction in any medium or format, as long as you give appropriate credit to the original author(s) and the source, provide a link to the Creative Commons licence, and indicate if changes were made. The images or other third party material in this article are included in the article's Creative Commons licence, unless indicated otherwise in a credit line to the material. If material is not included in the article's Creative Commons licence and your intended use is not permitted by statutory regulation or exceeds the permitted use, you will need to obtain permission directly from the copyright holder. To view a copy of this licence, visit <http://creativecommons.org/licenses/by/4.0/>.  
Funded by SCOAP<sup>3</sup>.

## References

- Supernova Cosmology Project Collaboration, S. Perlmutter et al., Discovery of a supernova explosion at half the age of the Universe and its cosmological implications, *Nature* **391**, 51–54 (1998). arXiv:astro-ph/9712212
- Supernova Search Team Collaboration, A.G. Riess et al., Observational evidence from supernovae for an accelerating universe and a cosmological constant. *Astron. J.* **116**, 1009–1038 (1998). arXiv:astro-ph/9805201
- Supernova Cosmology Project Collaboration, S. Perlmutter et al., Measurements of  $\Omega$  and  $\Lambda$  from 42 high redshift supernovae. *Astrophys. J.* **517**, 565–586 (1999). arXiv:astro-ph/9812133
- A. Wright, Nobel Prize 2011: Perlmutter, Schmidt & Riess. *Nat. Phys.* **7**, 833 (2011)
- S. Linden, J.M. Virey, A. Tilquin, Cosmological parameter extraction and biases from type Ia supernova magnitude evolution. *Astron. Astrophys.* **506**, 1095–1105 (2009)
- D. Camarena, V. Marra, A new method to build the (inverse) distance ladder. *Mon. Not. R. Astron. Soc.* **495**(3), 2630–2644 (2020). arXiv:1910.14125
- Pan-STARRS1 Collaboration, D.M. Scolnic et al., The Complete Light-curve Sample of Spectroscopically Confirmed SNe Ia from Pan-STARRS1 and Cosmological Constraints from the Combined Pantheon Sample. *Astrophys. J.* **859**(2), 101 (2018). arXiv:1710.00845
- A.K. Çamlıbel, I. Semiz, M.A. Feyizoğlu, Pantheon update on a model-independent analysis of cosmological supernova data. *Class. Quantum Gravity* **37**(23), 235001 (2020). arXiv:2001.04408
- Planck Collaboration, P.A.R. Ade et al., Planck 2013 results. XVI. Cosmological parameters. *Astron. Astrophys.* **571**, A16 (2014). arXiv:1303.5076
- Planck Collaboration, P.A.R. Ade et al., Planck 2015 results. XIII. Cosmological parameters. *Astron. Astrophys.* **594**, A13 (2016). arXiv:1502.01589
- Planck Collaboration, N. Aghanim et al., Planck 2018 results. VI. Cosmological parameters. *Astron. Astrophys.* **641**, A6 (2020) (Erratum: *Astron. Astrophys.* 652, C4 (2021)). arXiv:1807.06209
- R. Jimenez, A. Loeb, Constraining cosmological parameters based on relative galaxy ages. *Astrophys. J.* **573**, 37–42 (2002). arXiv:astro-ph/0106145
- A.M. Pinho, S. Casas, L. Amendola, Model-independent reconstruction of the linear anisotropic stress  $\eta$ . *JCAP* **11**, 027 (2018). arXiv:1805.00027
- S. Cao, B. Ratra,  $H_0=69.8\pm 1.3$  km s<sup>-1</sup> Mpc<sup>-1</sup>,  $\Omega_m=0.288\pm 0.017$ , and other constraints from lower-redshift, non-CMB, expansion-rate data. *Phys. Rev. D* **107**(10), 103521 (2023). arXiv:2302.14203
- BOSS Collaboration, S. Alam et al., The clustering of galaxies in the completed SDSS-III Baryon Oscillation Spectroscopic Survey: cosmological analysis of the DR12 galaxy sample. *Mon. Not. R. Astron. Soc.* **470**(3), 2617–2652 (2017). arXiv:1607.03155
- eBOSS Collaboration, S. Alam, et al., Completed SDSS-IV extended Baryon Oscillation Spectroscopic Survey: Cosmological implications from two decades of spectroscopic surveys at the Apache Point Observatory. *Phys. Rev. D* **103**(8), 083533 (2021). arXiv:2007.08991
- J. Hou et al., The completed SDSS-IV extended Baryon Oscillation spectroscopic survey: BAO and RSD measurements from anisotropic clustering analysis of the Quasar Sample in configuration space between redshift 0.8 and 2.2. *Mon. Not. R. Astron. Soc.* **500**(1), 1201–1221 (2020). arXiv:2007.08998
- P.J.E. Peebles, B. Ratra, The cosmological constant and dark energy. *Rev. Mod. Phys.* **75**, 559–606 (2003). arXiv:astro-ph/0207347
- E.J. Copeland, M. Sami, S. Tsujikawa, Dynamics of dark energy. *Int. J. Mod. Phys. D* **15**, 1753–1936 (2006). arXiv:hep-th/0603057
- J. Yoo, Y. Watanabe, Theoretical models of dark energy. *Int. J. Mod. Phys. D* **21**, 1230002 (2012). arXiv:1212.4726
- A.I. Lonappan, S. Kumar, B.R.R. Dinda, A.A. Sen, Bayesian evidences for dark energy models in light of current observational data. *Phys. Rev. D* **97**(4), 043524 (2018). arXiv:1707.00603
- B.R. Dinda, Probing dark energy using convergence power spectrum and bi-spectrum. *JCAP* **09**, 035 (2017). arXiv:1705.00657
- B.R. Dinda, A.A. Sen, T.R. Choudhury, Dark energy constraints from the 21 cm intensity mapping surveys with SKA1. arXiv:1804.11137
- T. Clifton, P.G. Ferreira, A. Padilla, C. Skordis, Modified gravity and cosmology. *Phys. Rep.* **513**, 1–189 (2012). arXiv:1106.2476
- K. Koyama, Cosmological tests of modified gravity. *Rep. Prog. Phys.* **79**(4), 046902 (2016). arXiv:1504.04623
- S. Tsujikawa, Modified gravity models of dark energy. *Lect. Notes Phys.* **800**, 99–145 (2010). arXiv:1101.0191
- A. Joyce, L. Lombriser, F. Schmidt, Dark energy versus modified gravity. *Ann. Rev. Nucl. Part. Sci.* **66**, 95–122 (2016). arXiv:1601.06133
- B.R. Dinda, M. Wali Hossain, A.A. Sen, Observed galaxy power spectrum in cubic Galileon model. *JCAP* **01**, 045 (2018). arXiv:1706.00567
- B.R. Dinda, Weak lensing probe of cubic Galileon model. *JCAP* **06**, 017 (2018). arXiv:1801.01741
- J. Zhang, B.R. Dinda, M.W. Hossain, A.A. Sen, W. Luo, Study of cubic Galileon gravity using  $N$ -body simulations. *Phys. Rev. D* **102**(4), 043510 (2020). arXiv:2004.12659
- B.R. Dinda, M.W. Hossain, A.A. Sen, 21 cm power spectrum in interacting cubic Galileon model. arXiv:2208.11560
- A. Bassi, B.R. Dinda, A.A. Sen, 21 cm Power spectrum for Bimetric gravity and its detectability with SKA1-Mid telescope. arXiv:2306.03875
- S. Nojiri, S.D. Odintsov, Unified cosmic history in modified gravity: from F(R) theory to Lorentz non-invariant models. *Phys. Rep.* **505**, 59–144 (2011). arXiv:1011.0544
- S. Nojiri, S.D. Odintsov, V.K. Oikonomou, Modified gravity theories on a nutshell: inflation, bounce and late-time evolution. *Phys. Rep.* **692**, 1–104 (2017). arXiv:1705.11098
- K. Bamba, S. Capozziello, S. Nojiri, S.D. Odintsov, Dark energy cosmology: the equivalent description via different theoretical models and cosmography tests. *Astrophys. Space Sci.* **342**, 155–228 (2012). arXiv:1205.3421
- B.-H. Lee, W. Lee, E.O. Colgáin, M.M. Sheikh-Jabbari, S. Thakur, Is local  $H_0$  at odds with dark energy EFT? *JCAP* **04**(04), 004 (2022). arXiv:2202.03906
- S.M. Carroll, The cosmological constant. *Living Rev. Relativ.* **4**, 1 (2001). arXiv:astro-ph/0004075

38. I. Zlatev, L.-M. Wang, P.J. Steinhardt, Quintessence, cosmic coincidence, and the cosmological constant. *Phys. Rev. Lett.* **82**, 896–899 (1999). arXiv:astro-ph/9807002
39. V. Sahni, A.A. Starobinsky, The Case for a positive cosmological Lambda term. *Int. J. Mod. Phys. D* **9**, 373–444 (2000). arXiv:astro-ph/9904398
40. H. Velten, R. vom Martens, W. Zimdahl, Aspects of the cosmological “coincidence problem”. *Eur. Phys. J. C* **74**(11), 3160 (2014). arXiv:1410.2509
41. M. Malquarti, E.J. Copeland, A.R. Liddle, K-essence and the coincidence problem. *Phys. Rev. D* **68**, 023512 (2003). arXiv:astro-ph/0304277
42. E. Di Valentino, O. Mena, S. Pan, L. Visinelli, W. Yang, A. Melchiorri, D.F. Mota, A.G. Riess, J. Silk, In the realm of the hubble tension – a review of solutions. arXiv:2103.01183
43. C. Krishnan, R. Mohayaee, E.O. Colgáin, M.M. Sheikh-Jabbari, L. Yin, Does Hubble tension signal a breakdown in FLRW cosmology? *Class. Quantum Gravity* **38**(18), 184001 (2021). arXiv:2105.09790
44. S. Vagnozzi, New physics in light of the  $H_0$  tension: an alternative view. *Phys. Rev. D* **102**(2), 023518 (2020). arXiv:1907.07569
45. B.R. Dinda, Cosmic expansion parametrization: implication for curvature and  $H_0$  tension. *Phys. Rev. D* **105**(6), 063524 (2022). arXiv:2106.02963
46. E. Di Valentino et al., Cosmology intertwined III:  $f\sigma_8$  and  $S_8$ . *Astropart. Phys.* **131**, 102604 (2021). arXiv:2008.11285
47. E. Abdalla et al., Cosmology intertwined: a review of the particle physics, astrophysics, and cosmology associated with the cosmological tensions and anomalies. *JHEAp* **34**, 49–211 (2022). arXiv:2203.06142
48. M. Douspis, L. Salvati, N. Aghanim, On the tension between large scale structures and cosmic microwave background. *PoS EDSU2018 037* (2018). arXiv:1901.05289
49. A. Bhattacharyya, U. Alam, K.L. Pandey, S. Das, S. Pal, Are  $H_0$  and  $\sigma_8$  tensions generic to present cosmological data? *Astrophys. J.* **876**(2), 143 (2019). arXiv:1805.04716
50. G. Bargiacchi, M.G. Dainotti, S. Capozziello, Tensions with the flat  $\Lambda$ CDM model from high-redshift cosmography. *Mon. Not. R. Astron. Soc.* **525**(2), 3104–3116 (2023). arXiv:2307.15359
51. B.S. Haridasu, V.V. Luković, M. Moresco, N. Vittorio, An improved model-independent assessment of the late-time cosmic expansion. *JCAP* **10**, 015 (2018). arXiv:1805.03595
52. R.C. Bernardo, J. Levi Said, Towards a model-independent reconstruction approach for late-time Hubble data. *JCAP* **08**, 027 (2021). arXiv:2106.08688
53. J.-J. Wei, F. Melia, Cosmology-independent estimate of the hubble constant and spatial curvature using time-delay lenses and quasars. *Astrophys. J.* **897**(2), 127 (2020). arXiv:2005.10422
54. D.M. Naik, N.S. Kavya, L. Sudharani, V. Venkatesha, Model-independent cosmological insights from three newly reconstructed deceleration parameters with observational data. *Phys. Lett. B* **844**, 138117 (2023)
55. S. Capozziello, P.K.S. Dunsby, O. Luongo, Model-independent reconstruction of cosmological accelerated-decelerated phase. *Mon. Not. R. Astron. Soc.* **509**(4), 5399–5415 (2021). arXiv:2106.15579
56. A.C. Alfano, C. Cafaro, S. Capozziello, O. Luongo, Dark energy-matter equivalence by the evolution of cosmic equation of state. *Phys. Dark Univ.* **42**, 101298 (2023). arXiv:2306.08396
57. S. Capozziello, O. Farooq, O. Luongo, B. Ratra, Cosmographic bounds on the cosmological deceleration-acceleration transition redshift in  $f(\mathcal{R})$  gravity. *Phys. Rev. D* **90**(4), 044016 (2014). arXiv:1403.1421
58. B.R. Dinda, Minimal model-dependent constraints on cosmological nuisance parameters and cosmic curvature from combinations of cosmological data. *Int. J. Mod. Phys. D* **32**(11), 2350079 (2023). arXiv:2209.14639
59. B.R. Dinda, N. Banerjee, Model independent bounds on type Ia supernova absolute peak magnitude. *Phys. Rev. D* **107**(6), 063513 (2023)
60. B.R. Dinda, Model independent parametrization of the late time cosmic acceleration: constraints on the parameters from recent observations. *Phys. Rev. D* **100**(4), 043528 (2019). arXiv:1904.10418
61. J. Ruiz-Zapatero, C. García-García, D. Alonso, P.G. Ferreira, R.D.P. Grumitt, Model-independent constraints on  $\Omega_m$  and  $H(z)$  from the link between geometry and growth. *Mon. Not. R. Astron. Soc.* **512**(2), 1967–1984 (2022). arXiv:2201.07025
62. F. Avila, A. Bernui, A. Bonilla, R.C. Nunes, Inferring  $S_8(z)$  and  $\gamma(z)$  with cosmic growth rate measurements using machine learning. *Eur. Phys. J. C* **82**(7), 594 (2022). arXiv:2201.07829
63. B. L’Huillier, A. Shafieloo, H. Kim, Model-independent cosmological constraints from growth and expansion. *Mon. Not. R. Astron. Soc.* **476**(3), 3263–3268 (2018)
64. S. Lee, Measuring the matter energy density and Hubble parameter from large scale structure. *JCAP* **02**, 021 (2014). arXiv:1307.6619
65. R.F.L. Holanda, R.S. Gonçalves, J.E. Gonzalez, J.S. Alcaniz, An estimate of the dark matter density from galaxy clusters and supernovae data. *JCAP* **11**, 032 (2019). arXiv:1905.09689
66. C. Williams, C. Rasmussen, Gaussian processes for regression. *Adv. Neural Inf. Process. Syst.* **8** (1995)
67. C.E. Rasmussen, C.K.I. Williams, *Gaussian Processes for Machine Learning*, 2nd edn. (The MIT Press, Cambridge, 2006)
68. M. Seikel, C. Clarkson, M. Smith, Reconstruction of dark energy and expansion dynamics using gaussian processes. *J. Cosmol. Astropart. Phys.* **2012**, 036–036 (2012)
69. A. Shafieloo, A.G. Kim, E.V. Linder, Gaussian process cosmography. *Phys. Rev. D* **85**, 123530 (2012)
70. S.-G. Hwang, B. L’Huillier, R.E. Keeley, M.J. Jee, A. Shafieloo, How to use GP: effects of the mean function and hyperparameter selection on Gaussian Process regression. arXiv:2206.15081
71. R.E. Keeley, A. Shafieloo, G.-B. Zhao, J.A. Vazquez, H. Koo, Reconstructing the universe: testing the mutual consistency of the Pantheon and SDSS/eBOSS BAO data sets with gaussian processes. *Astron. J.* **161**(3), 151 (2021)
72. L. Perenon, M. Martinelli, R. Maartens, S. Camera, C. Clarkson, Measuring dark energy with expansion and growth. *Phys. Dark Univ.* **37**, 101119 (2022). arXiv:2206.12375
73. L. Perenon, M. Martinelli, S. Ilić, R. Maartens, M. Lochner, C. Clarkson, Multi-tasking the growth of cosmological structures. *Phys. Dark Univ.* **34**, 100898 (2021). arXiv:2105.01613
74. E.Ó. Colgáin, M.M. Sheikh-Jabbari, Elucidating cosmological model dependence with  $H_0$ . *Eur. Phys. J. C* **81**(10), 892 (2021). arXiv:2101.08565
75. N. Banerjee, P. Mukherjee, D. Pavón, Checking the second law at cosmic scales. *JCAP* **11**, 092 (2023). arXiv:2309.12298
76. N. Banerjee, P. Mukherjee, D. Pavón, Spatial curvature and thermodynamics. *Mon. Not. R. Astron. Soc.* **521**(4), 5473–5482 (2023). arXiv:2301.09823
77. P. Mukherjee, N. Banerjee, Constraining the curvature density parameter in cosmology. *Phys. Rev. D* **105**(6), 063516 (2022). arXiv:2202.07886
78. P. Mukherjee, N. Banerjee, Revisiting a non-parametric reconstruction of the deceleration parameter from combined background and the growth rate data. *Phys. Dark Univ.* **36**, 100998 (2022). arXiv:2007.15941
79. P. Mukherjee, N. Banerjee, Non-parametric reconstruction of the cosmological *jerk* parameter. *Eur. Phys. J. C* **81**(1), 36 (2021). arXiv:2007.10124

80. E.-K. Li, M. Du, Z.-H. Zhou, H. Zhang, L. Xu, Testing the effect of  $H_0$  on  $f\sigma_8$  tension using a Gaussian process method. *Mon. Not. R. Astron. Soc.* **501**(3), 4452–4463 (2021). arXiv:1911.12076
81. J. Ruiz-Zapatero, D. Alonso, P.G. Ferreira, C. Garcia-Garcia, Impact of the Universe's expansion rate on constraints on modified growth of structure. *Phys. Rev. D* **106**(8), 083523 (2022). arXiv:2207.09896
82. Z. Sakr, Testing the hypothesis of a matter density discrepancy within  $\Lambda$ CDM model using multiple probes. *Phys. Rev. D* **108**(8), 083519 (2023). arXiv:2305.02846
83. B.R. Dinda, N. Banerjee, Constraints on the speed of sound in the k-essence model of dark energy. arXiv:2309.10538
84. B.R. Dinda, Nonlinear power spectrum in clustering and smooth dark energy models beyond the BAO scale. *J. Astrophys. Astron.* **40**(2), 12 (2019). arXiv:1804.07953
85. M. Moresco, R. Jimenez, L. Verde, A. Cimatti, L. Pozzetti, Setting the stage for cosmic chronometers. II. Impact of stellar population synthesis models systematics and full covariance matrix. *Astrophys. J.* **898**(1), 82 (2020). arXiv:2003.07362
86. M. Moresco, A. Cimatti, R. Jimenez, L. Pozzetti, G. Zamorani, M. Bolzonella, J. Dunlop, F. Lamareille, M. Mignoli, H. Pearce, et al., Improved constraints on the expansion rate of the universe up to  $z$  1.1 from the spectroscopic evolution of cosmic chronometers. *J. Cosmol. Astropart. Phys.* **2012**(08), 006 (2012)
87. M. Moresco, Raising the bar: new constraints on the Hubble parameter with cosmic chronometers at  $z \sim 2$ . *Mon. Not. R. Astron. Soc.* **450**(1), L16–L20 (2015). arXiv:1503.01116
88. M. Moresco, L. Pozzetti, A. Cimatti, R. Jimenez, C. Maraston, L. Verde, D. Thomas, A. Citro, R. Tojeiro, and D. Wilkinson, A 6% measurement of the Hubble parameter at  $z \sim 0.45$ : direct evidence of the epoch of cosmic re-acceleration. *JCAP* **05**, 014 (2016). arXiv:1601.01701
89. C. Zhang, H. Zhang, S. Yuan, S. Liu, T.-J. Zhang, Y.-C. Sun, Four new observational  $h(z)$  data from luminous red galaxies in the sloan digital sky survey data release seven. *Res. Astron. Astrophys.* **14**(10), 1221 (2014)
90. J. Simon, L. Verde, R. Jimenez, Constraints on the redshift dependence of the dark energy potential. *Phys. Rev. D* **71**, 123001 (2005). arXiv:astro-ph/0412269
91. A.L. Ratsimbazafy, S.I. Loubser, S.M. Crawford, C.M. Cress, B.A. Bassett, R.C. Nichol, P. Väisänen, Age-dating luminous red galaxies observed with the Southern African large telescope. *Mon. Not. R. Astron. Soc.* **467**(3), 3239–3254 (2017). arXiv:1702.00418
92. D. Stern, R. Jimenez, L. Verde, M. Kamionkowski, S.A. Stanford, Cosmic chronometers: constraining the equation of state of dark energy. I:  $H(z)$  measurements. *J. Cosmol. Astropart. Phys.* **2010**(02), 008 (2010)
93. N. Borghi, M. Moresco, A. Cimatti, Toward a better understanding of cosmic chronometers: a new measurement of  $H(z)$  at  $z \sim 0.7$ . *Astrophys. J. Lett.* **928**(1), L4 (2022). arXiv:2110.04304
94. F. Avila, A. Bernui, E. de Carvalho, C.P. Novaes, The growth rate of cosmic structures in the local Universe with the ALFALFA survey. *Mon. Not. R. Astron. Soc.* **505**(3), 3404–3413 (2021). arXiv:2105.10583
95. E. Hawkins et al., The 2dF Galaxy Redshift Survey: correlation functions, peculiar velocities and the matter density of the universe. *Mon. Not. R. Astron. Soc.* **346**, 78 (2003). arXiv:astro-ph/0212375
96. L. Guzzo et al., A test of the nature of cosmic acceleration using galaxy redshift distortions. *Nature* **451**, 541–545 (2008). arXiv:0802.1944
97. C. Blake et al., Galaxy And Mass Assembly (GAMA): improved cosmic growth measurements using multiple tracers of large-scale structure. *Mon. Not. R. Astron. Soc.* **436**, 3089 (2013). arXiv:1309.5556
98. C. Blake, S. Brough, M. Colless, C. Contreras, W. Couch, S. Croom, T. Davis, M.J. Drinkwater, K. Forster, D. Gilbank, M. Gladders, K. Glazebrook, B. Jelliffe, R.J. Jurek, I.-H. Li, B. Madore, D.C. Martin, K. Pimbblet, G.B. Poole, M. Pracy, R. Sharp, E. Wisnioski, D. Woods, T.K. Wyder, H.K. C. Yee, The wigglez dark energy survey: the growth rate of cosmic structure since redshift  $z=0.9$ : Wigglez survey: growth of structure. *Mon. Not. R. Astron. Soc.* **415**, 2876–2891 (2011)
99. SDSS Collaboration, M. Tegmark et al., Cosmological constraints from the SDSS Luminous Red Galaxies. *Phys. Rev. D* **74**, 123507 (2006). arXiv:astro-ph/0608632
100. N.P. Ross et al., The 2dF-SDSS LRG and QSO Survey: the 2-point correlation function and Redshift-Space distortions. *Mon. Not. R. Astron. Soc.* **381**, 573–588 (2007). arXiv:astro-ph/0612400
101. J. da Angela et al., The 2dF-SDSS LRG and QSO Survey: QSO clustering and the  $L$ - $z$  degeneracy. *Mon. Not. R. Astron. Soc.* **383**, 565–580 (2008). arXiv:astro-ph/0612401
102. S. Cao, J. Qi, Z. Cao, M. Biesiada, J. Li, Y. Pan, Z.-H. Zhu, Direct test of the FLRW metric from strongly lensed gravitational wave observations. *Sci. Rep.* **9**(1), 11608 (2019). arXiv:1910.10365
103. Y. Liu, S. Cao, T. Liu, X. Li, S. Geng, Y. Lian, W. Guo, Model-independent constraints on cosmic curvature: implication from updated Hubble diagram of high-redshift standard candles. *Astrophys. J.* **901**(2), 129 (2020). arXiv:2008.08378
104. W.L. Freedman et al., The Carnegie-Chicago Hubble Program. VIII. An independent determination of the Hubble constant based on the tip of the red giant branch. *Astrophys. J.* **882** 34 (2019). arXiv:1907.05922
105. A.G. Riess, S. Casertano, W. Yuan, J.B. Bowers, L. Macri, J.C. Zinn, D. Scolnic, Cosmic distances calibrated to 1% precision with Gaia EDR3 parallaxes and Hubble Space Telescope photometry of 75 Milky Way Cepheids confirm tension with  $\Lambda$ CDM. *Astrophys. J. Lett.* **908**(1), L6 (2021). [arXiv:2012.08534]